MSDE

PAPER

View Article Online
View Journal | View Issue

Cite this: *Mol. Syst. Des. Eng.*, 2023, **8**, 1526

Evaluating the CO_2 capture performance of a "phase-change" metal–organic framework in a pressure-vacuum swing adsorption process†

David Danaci, *[a] Elena Pulidori,[b] Luca Bernazzani, [b] Camille Petit [a] and Marco Taddei *[bc]

Metal–organic frameworks (MOFs) that display step-shaped adsorption isotherms, *i.e.*, "phase-change" MOFs, represent a relatively small subset of all known MOFs. Yet, they are rapidly emerging as promising sorbents to achieve excellent gas separation performances with little energy demand. In this work, we assessed F4_MIL-140A(Ce), a recently discovered "phase-change" MOF adsorbent, for CO_2 capture in two scenarios using a pressure-vacuum swing adsorption process, namely a coal-fired power plant flue gas (12.5%$_{mol}$ CO_2), and a steel plant flue gas (25.5%$_{mol}$ CO_2). Four CO_2 and three N_2 adsorption isotherms were collected on F4_MIL-140A(Ce) over a range of temperatures and modelled using a bespoke equation for step-shaped isotherms. We accurately measured the heat capacity of F4_MIL-140A(Ce), a key thermodynamic property for a sorbent, using a method based on differential scanning calorimetry that overcomes the issues associated with the poor thermal conductivity of MOF powders. We then used these experimental data as input in a process optimisation framework and we compared the CO_2 capture performance of F4_MIL-140A(Ce) to that of other "canonical" sorbents, including, zeolite 13X, activated carbon and three MOFs (*i.e.*, HKUST-1, UTSA-16 and CALF-20). We found that F4_MIL-140A(Ce) has the potential to perform better than other sorbents, in terms of recovery and purity, under most of the simulated process conditions. We attribute such promising performance to the non-hysteretic step-shaped isotherm, the low uptake capacity for N_2 and the mild heat of CO_2 adsorption displayed by F4_MIL-140A(Ce).

Received 14th June 2023,
Accepted 4th September 2023

DOI: 10.1039/d3me00098b

rsc.li/molecular-engineering

Design, System, Application

"Phase-change" metal–organic frameworks (MOFs) that display step-shaped adsorption isotherms are seen as an emerging class of solid sorbents for energy efficient gas separation processes. The step-shaped isotherm can, in principle, afford high working capacity and selectivity, provided that the sorbent operates under process conditions that allow taking full advantage of the peculiar shape of the isotherm. In a pressure-vacuum swing adsorption process occurring under adiabatic conditions, the shift of the step to higher or lower pressures in response to temperature changes can heavily impact the cyclic performance. A key role in such context is played by thermodynamic properties of the sorbent, *i.e.*, heat of adsorption and specific heat capacity, which determine the extent to which the step will shift between the adsorption and the desorption stage. In this article, we assess the potential of F4_MIL-140A(Ce), a recently discovered "phase-change" MOF that displays non-hysteretic step-shaped CO_2 adsorption isotherm, for post-combustion CO_2 capture in a pressure-vacuum swing adsorption process, against other zeolite, activated carbon and MOF benchmark sorbents.

Introduction

The urgent need to decarbonise power production and industrial activities worldwide is calling for efforts by scientists and engineers to develop and deploy novel technologies for CO_2 emission reduction in the short term. In this context, carbon capture and storage can serve as a bridge technology, helping to dampen the environmental impact of fossil fuels while they are displaced by other energy sources.[1] CO_2 capture using adsorption-based processes is not yet competitive with the state-of-the-art technology based

[a] *Barrer Centre, Department of Chemical Engineering, Imperial College London, London, SW7 2AZ, UK. E-mail: david.danaci@imperial.ac.uk*
[b] *Dipartimento di Chimica e Chimica Industriale, Unità di Ricerca INSTM, Università di Pisa, Via Giuseppe Moruzzi 13, 56124 Pisa, Italy. E-mail: marco.taddei@unipi.it*
[c] *Energy Safety Research Institute, Swansea University, Fabian Way, Swansea, SA1 8EN, UK*

† Electronic supplementary information (ESI) available. See DOI: https://doi.org/10.1039/d3me00098b

on aqueous amine absorbents.[1–3] Yet, solid adsorbents offer potential advantages, in terms of energy intensity and recyclability, which make them the object of intense research. Candidate porous solid adsorbents include zeolites, activated carbons, amine-functionalised porous silicas and metal–organic frameworks (MOFs).[2–5] MOFs benefit from unparalleled structural versatility, tunability of the physicochemical properties and can display unique adsorption mechanisms. An example are the so-called "phase-change" MOFs, a small subset of MOFs that display step-shaped isotherms, *i.e.*, they take up large amounts of gas when a threshold partial pressure of the adsorbate is reached.[6–9] This peculiar behaviour is associated with a phase transition in the sorbent and can, in principle, lead to an optimal compromise in terms of achievable working capacity, selectivity and mild regeneration conditions.[6,10,11] There have been several prior studies examining MOFs for post-combustion CO_2 capture applications under PVSA conditions.[12–19] Until very recently, a "phase-change" MOF had not been investigated in this scenario.[20]

Amine-appended MOFs with isoreticularly expanded MOF-74 structure are perhaps the most widely known class of "phase-change" MOFs for CO_2 capture.[6,21–24] The general formula for these MOFs is M^{II}_2(dobpdc), where M^{II} is a divalent metal (Mg, Mn, Fe, Co, Ni, Zn) and dobpdc^{4-} is 4,4′-dioxido-3,3′-biphenyldicarboxylate. Aliphatic diamines are coordinated to the metal ions and CO_2 is adsorbed with a cooperative mechanism that involves its insertion between an amine group and a metal ion, with formation of a metal-carbamate adduct and a hydrogen bond with a neighbouring amine group.[6] The position of the step in the isotherm can be modulated by changing the metal ion, as this influences the bond strength with the amine and, in turn, the ease with which CO_2 can be inserted in between them. Hefti and Joss *et al.*[10] investigated for the first time the post-combustion CO_2 capture performance of *N*,*N*′-dimethylethylenediamine(mmen)-appended MOFs in a four-stage temperature swing adsorption (TSA) process. They found that the Mn^{II}-based MOF is the best performing one, as it can simultaneously fulfil the requirements for recovery (90%) and purity (95%) with an energy consumption lower than the benchmark zeolite 13X. More recently, Pai *et al.*[25] evaluated the same MOFs for CO_2 capture by vacuum swing adsorption (VSA), finding that the Mn^{II}-based MOF represents again the best compromise between performance and cost. Another recent study reports on the techno-economic analysis of a TSA process involving a Mg^{II}-based MOF with appended 2,2-dimethyl-1,3-diaminopropane (dmpn).[26] This study highlighted the big impact of heat management on process metrics and, in turn, on the associated costs, identifying a "modified" TSA process that involves cooling and heating with water as a promising approach to mitigate this issue.

Another class of "phase-change" CO_2 sorbents is the so-called elastic layered materials (ELMs), with the general formula $Cu^{II}(bipy)_2(X)_2$, where bipy is 4,4′-bipyridine and X^- is a weakly coordinating anion, *e.g.*, BF^{4-} or CF_3SO^{3-}. ELM-11, the most representative member of this class of compounds, is constituted of square layers built from the coordination of Cu^{II} ions, bipy and BF^{4-}, stacked on top of each other.[8,27–29] The adsorption of CO_2 in ELM-11 occurs *via* cooperative intercalation between the layers, leading to a significant increase of volume of the unit cell.[30] Such a mechanism entails that desorption occurs at a lower pressure than adsorption, yielding a hysteretic isotherm. This trait is common to other MOFs exhibiting flexible behaviour, such as breathing.[31,32] The performance of ELM-11 for CO_2 capture by pressure-vacuum swing adsorption (PVSA) has been recently evaluated by Takakura *et al.*,[20] who observed that it can outperform zeolite 13X in terms of recovery, purity and energy consumption, while requiring a smaller bed size.

F4_MIL-140A(Ce) is a recently discovered ultramicroporous "phase-change" MOF with the formula $Ce^{IV}O$(tfbdc), where tfbdc^{2-} is tetrafluoroterephthalate, whose crystal structure (Fig. S1†) features triangular channels running along the *c*-axis direction, lined by the fluorine atoms of the linker.[33,34] It displays a non-hysteretic step-shaped CO_2 adsorption isotherm, with steep uptake increase at pressure <0.2 bar at 298 K, allowing saturation to be reached within a narrow range of pressure (Fig. S2 and S3†).[33] This behaviour originates from the concerted rotation of perfluorinated aromatic rings, which opens the gate to a highly favourable adsorption site, where CO_2 interacts with both open coordination sites on the metal atoms and fluorine atoms on the organic linker.[35] The N_2 adsorption isotherm displays almost negligible uptake in the same pressure range, leading to an ultrahigh calculated CO_2/N_2 selectivity. Interestingly, F4_MIL-140A(Ce) can conveniently be synthesised from commercially available reagents under mild conditions and in aqueous medium, with potential for production on a large scale.

In light of the promising CO_2 adsorption properties of F4_MIL-140A(Ce), in this work, we set out to evaluate its performance as a sorbent for post-combustion CO_2 capture in a range of scenarios by pressure-vacuum swing adsorption (PVSA).

Results and discussion

The PVSA model used herein requires adsorption isotherms as a function of temperature and pressure for CO_2 and N_2, the density and void fraction of the bed, and the adsorbent heat capacity as inputs. Below, we detail how we measured or estimated these properties for F4_MIL-140A(Ce).

CO_2 and N_2 sorption

The measured CO_2 and N_2 isotherms for F4_MIL-140A(Ce) are shown in Fig. 1, with the corresponding fitted isotherm parameters in Table 1. Due to the shape of the isotherms, the stepped isotherm model proposed by Hefti and Joss *et al.*[10] is used.

As for other adsorbents with stepped isotherms, the step pressure increases to a higher pressure with temperature.[6,7,9,20,22] Like MIL-53(Al),[36] a prototypical "phase-change" adsorbent, N_2

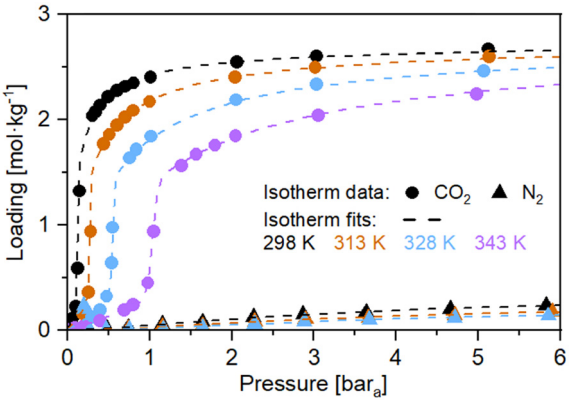

Fig. 1 Excess adsorption isotherms for F4_MIL-140A(Ce) and accompanying isotherm model fits. CO_2 (circles), N_2 (triangles), isotherm model (dashed lines), and temperatures are represented by colours, 298 K (black), 313 K (orange), 328 K (light blue), 343 K (lavender).

Table 1 F4_MIL-140A(Ce) isotherm fitting parameters for the stepped isotherm model proposed by Hefti and Joss *et al.*[10] The units are as follows: T_0 – K, $p_{step,0}$ – bar, H_{step} – J mol^{-1}, n_i^{∞} – mol kg^{-1}, b_i^{∞} – bar^{-1}, and E_i – J mol^{-1}. χ and γ are unitless. The reader is directed to Hefti and Joss *et al.*[10] for further details on the isotherm model equations and interpretation of the parameters

	CO_2	N_2
T_0	2.5315×10^{2}	2.5315×10^{2}
$p_{step,0}$	7.5420×10^{-3}	7.1356×10^{-1}
H_{step}	3.9776×10^{4}	0.0000×10^{0}
χ_1	1.2330×10^{-2}	1.0053×10^{1}
χ_2	6.6055×10^{2}	0.0000×10^{0}
n_L^{∞}	1.5020×10^{2}	1.1810×10^{1}
b_L^{∞}	1.6174×10^{-9}	1.2135×10^{-10}
E_L	3.9772×10^{4}	4.2444×10^{4}
n_U^{∞}	2.6572×10^{0}	2.4511×10^{-1}
b_U^{∞}	3.3204×10^{-7}	3.0922×10^{-10}
E_U	4.2735×10^{4}	6.2986×10^{4}
b_H^{∞}	1.3344×10^{-3}	1.1786×10^{-5}
E_H	4.1670×10^{3}	0.0000×10^{0}
Γ	4.6714×10^{-1}	5.6688×10^{0}

does not show a stepped isotherm under the same measurement conditions as CO_2. However, a key difference to MIL-53(Al) is that when the step occurs, F4_MIL-140A(Ce) does not show any hysteresis during desorption (Fig. S2–S4†). This feature is particularly useful for adsorption processes, as desorption hysteresis impedes adsorbate recovery. On initial inspection, the alignment of the CO_2 isotherm steps appears convenient for post-combustion CO_2 capture applications, ranging between ≈0.13 bar_a and ≈1.05 bar_a at temperatures 298 K to 343 K.

For this work, in the absence of binary adsorption data, we assume that the N_2 loading (and thus selectivity) is not impacted by the step in the CO_2 loading. Considering this assumption for F4_MIL-140A(Ce) results in some degree of overestimating the product purity. Based on the limited multicomponent adsorption data in the literature, which is even more limited for materials that display a transition in the isotherm, this assumption has not been verified for some other systems.[37–39] In these other systems, the step in the isotherm is accompanied by a change in crystal volume. However, based on our other work,[35] the volume of F4_MIL-140A(Ce) is not impacted by the isotherm step. Thus, additional surface area, or increase in pore size is not seen, which would promote the adsorption of N_2. Therefore, this assumption may not be completely invalid in the case of F4_MIL-140A(Ce).

Density and void fraction

The density of an adsorbent and the void fraction of the bed also play a role in process performance. The density governs how much volume will be occupied by a given mass of adsorbent. High densities are preferable as they lead to smaller vessels and a lower pressure drop. A lower pressure drop is especially valuable in the case of VSA processes, both for the adsorption stage, where it minimises the feed blower energy requirement, and for the desorption stage, to minimise the time required to achieve the desired vacuum at the opposite end of the bed (and subsequently, energy). F4_MIL-140A(Ce) has a crystal density of 2.23 g cm^{-3} in its evacuated form,[35] a value that is significantly higher than most MOFs, including those evaluated here (UTSA-16 = 1.66 g cm^{-3};[40] CALF-20 = 1.70 g cm^{-3};[41] HKUST-1 = 0.96 g cm^{-3}).[42] This high density is the result of the combination between the high formula weight of F4_MIL-140A(Ce) (392 g mol^{-1} for the evacuated form) and its small pore volume (0.10 cm^3 g^{-1}). Based on the literature,[43] we have assumed here that the density of a pellet of F4_MIL-140A(Ce) is 80% of the crystallographic density of the evacuated form.

The total void fraction of the bed is composed of two components, the interstitial voids between particles (*i.e.*, packing fraction, or interparticle void space) and the porosity of the adsorbent itself (*i.e.*, total pore volume, or intraparticle void space). Void space does not contribute to the separation and can hamper product purity, so it should be minimised. The packing fraction is not easily reduced, this means that any reduction should stem from the adsorbent particles/pellets.

Therefore, the ideal is to maximise adsorbent pellet density and minimise the pellet void fraction. This is especially important for high-pressure applications where the adsorbent loading may become saturated at low pressures, but the void volume will continue to store feed gas as the pressure increases. In some cases, the void volume could store more gas than is adsorbed on the adsorbent; it is generally undesirable and should be avoided.

Heat capacity

The accurate measurement of the heat capacity (C_p) of an adsorbent is an essential step to obtain a reliable performance evaluation from process modelling, as this fundamental thermodynamic property has an impact on the achievable working capacity and, in turn, on recovery, purity

and productivity.[44–47] When determining the working capacity of a given adsorbent in a PVSA process, ideal isothermal conditions are often assumed. Under such ideal conditions, a single sorption isotherm at a given temperature, T, is in principle enough to determine the working capacity by simply calculating the difference between the equilibrium uptake at the partial pressure of gas under adsorption conditions (P_{ads}, high P) and the uptake at the partial pressure under desorption conditions (P_{des}, low P). Provided that P_{ads} and P_{des} lie above and below the inflection point, respectively, the "phase-change" adsorbent has the potential to achieve a much larger working capacity thanks to its step-shaped isotherm (Fig. S4†). However, a real PVSA process occurs under nearly adiabatic conditions, *i.e.*, with little or no exchange of heat between the adsorbent bed and the environment. Thus, the bed temperature will in fact swing between $T + \Delta T$ in the adsorption stage (exothermic) and $T - \Delta T$ in the desorption stage (endothermic), leading to a decreased gas uptake in the former stage and to an increased gas retention in the latter.[46,48] This will decrease the achievable working capacity, as shown in Fig. 2. The potential decrease in working capacity from the ideal isothermal case is much larger for a "phase-change" adsorbent than for a Langmuir-type one, as the inflection point of the step-shaped isotherm will shift to higher pressure in adsorption and to lower pressure in desorption. Such a shift could even make the adsorbent completely ineffective if P_{ads} and P_{des} are below and above the inflection point, respectively.

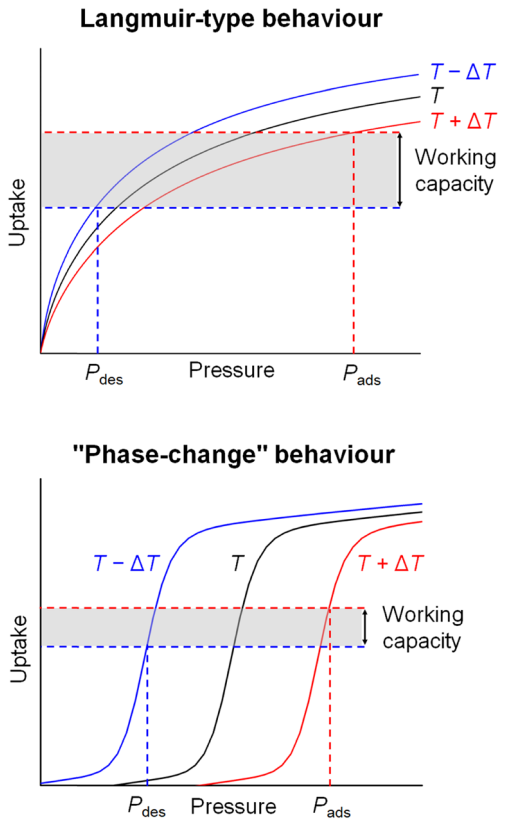

Fig. 2 Effect of the temperature swing upon adsorption ($T + \Delta T$, red isotherm) and desorption ($T - \Delta T$, blue isotherm) under adiabatic conditions on the working capacity of a sorbent displaying Langmuir-type behaviour (top) and one displaying "phase-change" behaviour (bottom). The ideal isothermal case is presented in Fig. S4.†

The extent of ΔT depends on both the heat of adsorption (Q_{ads}) and C_p: to minimise the thermal swing, the ideal sorbent should feature low Q_{ads} and high C_p. The Q_{ads} for CO_2 of F4_MIL-140A(Ce) was recently measured by adsorption microcalorimetry at 303 K, finding that it reaches a steady value of about 35 kJ mol^{-1} in the region of loading corresponding with the step in the isotherm.[35] Such a value is within the physisorption domain and in between those observed for amine-appended MOFs (about 70 kJ mol^{-1} for mmen-appended MOFs based on Mg^{II} and Mn^{II})[6] and ELM-11 (about 20 kJ mol^{-1}).[49] The value of isosteric Q_{ads} derived by applying the Clausius–Clapeyron equation (ranging between 40 and 42 kJ mol^{-1}) and used in the process modelling herein is slightly overestimated (Fig. S5†), if compared with the value obtained from microcalorimetry. The C_p of MOFs can be calculated using the molar heat capacity of the metal atoms from Rumble,[50] and approximating the molar heat capacity of the organic ligands at 313.15 K following the method described by Goodman *et al.*[51] By applying this method, we estimated a value of 748 J K^{-1} kg^{-1} for F4_MIL-140A(Ce) at 313.15 K. This method, though, is associated with a series of uncertainties affecting the value of C_p. In addition, it does not capture the variation of C_p as a function of temperature. Therefore, we set out to experimentally determine the C_p of F4_MIL-140A(Ce) over a range of temperature compatible with a real-life PVSA process.

We employed the standard three-run ASTM E1269-11 protocol,[52] based on differential scanning calorimetry (DSC) (see the Experimental section for more details). Analogous approaches were used in the sparse literature for the determination of the C_p of other MOFs.[53–56] The ASTM protocol involves heating a sample of mass in the range of 15–20 mg at a rate comprised between 10 and 20 K min^{-1} to ensure that the measured heat flow is sufficiently higher than the baseline, *i.e.*, the heat flow to an empty pan. The C_p of the sample is then determined based on the comparison with a sapphire reference sample with known C_p (see the Experimental section for further details). It is to be noted that the DSC instrument used for the measurements herein transfers heat by contact between a heating element and the flat bottom of aluminium pans.

Our initial attempts were carried out by heating samples of free flowing F4_MIL-140A(Ce) powder at a 10 K min^{-1} rate in the 273–483 K range. During the first heating ramp, two endothermic events were observed, associated with the loss of weakly physisorbed water (below 373 K) and coordinated water (above 373 K), respectively (Fig. S6†). Thermogravimetric analysis revealed that in this temperature range the solid lost 7.1% of the original mass (Fig. S7†). We observed a large

discrepancy between the obtained C_p values from samples having a mass of 4.06 mg and 1.84 mg, respectively, with the latter displaying nearly doubled C_p values (Fig. S8†). Given that C_p is an intensive property, such an apparently absurd result can be explained by the poor conductive character of MOFs, which display typical thermal conductivity, κ, values in the range of 0.1–1.0 W m^{-1} K^{-1}.[48] We hypothesise that heat transfer between the powder in direct contact with the pan surface and the rest of the powder is too slow compared with the heating rate, thus preventing the bulk of the sample from reaching thermal homogeneity. As a result, the heat flow measured by the calorimeter is lower than the theoretical one, leading to determination of a lower value of C_p than the actual one. Such an effect becomes obviously more marked in the sample with the largest mass, where the powder in direct contact with the pan represents a lower fraction of the total amount. Compression of the powder into thin pellets led to an increase in the value of C_p for both the sample with the highest mass (4.15 mg) and the one with the lowest mass (1.85 mg), suggesting that better contact between the MOF particles helped in improving heat transfer (Fig. S9–S11†). The extent of the increase was smaller for the sample with a mass of about 1.8 mg, suggesting that this sample was already closer to achieving thermal equilibrium during the measurement.

We argued that issues with heat transfer could be further minimised by dispersing the MOF powder within a matrix of high thermal conductivity. Liu *et al.*[55] recently reported that composites of MOF-5 (κ = 0.1 W m^{-1} K^{-1}) containing 1–10 wt% of expanded natural graphite (κ = 150 W m^{-1} K^{-1}) exhibit up to nine-fold enhancement in κ. As a matrix, we chose neutral activated alumina, commonly used as a stationary phase for chromatographic separations. Activated alumina displays high κ (36 W m^{-1} K^{-1} at 300 K)[57] and is in the form of a very fine powder, which allows the MOF to be finely dispersed and pellets to be easily prepared. We measured the C_p of a piece of a pellet of pure activated alumina, finding that it displays a similar value to that of the sapphire reference sample, in agreement with the fact that both samples are aluminium oxide (Fig. S12 and S13†). Then, we prepared pellets containing 10 and 20 wt% of F4_MIL-140A(Ce) dispersed within a matrix of activated alumina. To minimise mechanical damage to the MOF, a pressure of about 250 MPa was used to compress the powders. The heat flow measured with these samples (fragments of about 40 mg taken from each pellet) is the result of contributions due to both the activated alumina and the MOF (Fig. S14 and S15†), therefore the contribution of the MOF was determined by subtracting the contribution of pure activated alumina in the hypothesis of perfect additive behaviour of C_p. Averaged heat flows on two consecutive runs (with relative standard deviation lower than 2%) were employed for the calculation of C_p (see the Experimental section for additional details). The C_p values of F4_MIL-140A(Ce) obtained from the pellet containing 10 wt% of MOF and that containing 20 wt% of MOF were found to be in good agreement with each other (Fig. 3). The two curves are well described by a linear model

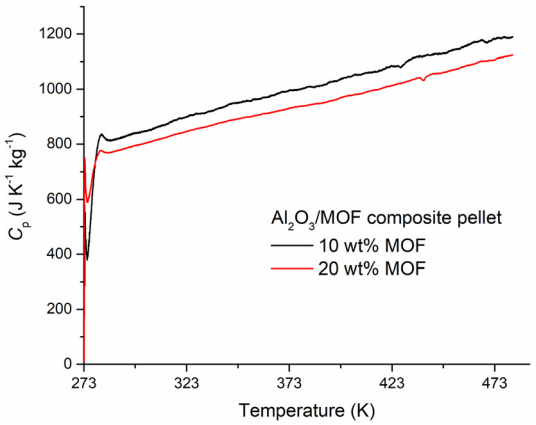

Fig. 3 Comparison between the C_p values in the 273–480 K temperature range obtained for composite pellets containing either 10 wt% (black) or 20 wt% (red) of F4_MIL-140A(Ce) dispersed in activated alumina.

in the 285–480 K range, with correlation coefficients >0.98 (Fig. S16 and S17†). The results of the sample containing 20 wt% of the MOF were chosen as the input for process modelling, as it was considered the most reliable one, due to the larger mass of the MOF (6.90 mg) and the consequently lower uncertainty on the value of C_p. In the 285–480 K range, C_p increases from 775 to 1119 J K^{-1} kg^{-1}. At 313.15 K, the C_p value is 824 J K^{-1} kg^{-1}, that is, 10% higher than the estimated one of 748 J K^{-1} kg^{-1}.

Process modelling

Modelling approach. Using the input data discussed above, we then assessed the performance of F4_MIL-140A(Ce) in two post-combustion CO_2 capture scenarios: a coal-fired power plant flue gas (12.5%$_{mol}$ CO_2), and a steel plant flue gas (25.5%$_{mol}$ CO_2). The flue gas was treated as a binary CO_2/N_2 mixture. Details as to how the flue gas compositions were determined can be found in our previous work.[44] We selected these streams based on inspection of the F4_MIL-140A(Ce) CO_2 isotherm steps and identifying common post-combustion capture applications that have CO_2 partial pressures in that range. Since we aimed to investigate the impact of the step in the CO_2 isotherm, we did not consider a natural gas-fired power plant flue gas (4.38%$_{mol}$ CO_2), as even under the PSA conditions considered in this work (see below), the isotherm step would not be able to be traversed.

To further examine the impact of the CO_2 isotherm step on performance, we considered three cycle operating schemes: pressure swing adsorption (PSA), pressure-vacuum swing adsorption (PVSA), and vacuum swing adsorption (VSA). Although all scenarios are within the remit of pressure swing adsorption, segregating the operating condition bounds in this way can help to highlight their impact. The allowed bounds of the operating conditions (adsorption temperature and cycle pressures) are summarised in Table 2. Traditionally, PSA has not been considered for post-

Table 2 Upper and lower optimiser bounds for the adsorption temperature and operating pressures for each cycle type

	PSA	PVSA	VSA
$T_{ads,min}$ [K]	293.15		
$T_{ads,max}$ [K]	373.15		
P_{max} [bar_a]	10	10	1.5
P_{min} [bar_a]	1.05	0.30	0.01

combustion CO_2 capture, due to the large volumes of flue gas typically encountered and the limitations of available compressors. However, the increased demand for larger cryogenic air separation units in the 5000–7000 tpd_{O_2} capacity range has driven the development of very large main air compressors (*e.g.*, MAN MAX1 series). Therefore, compressing large volumes of low-pressure flue gas is now technically feasible and may be worth investigating. PSA also offers the advantage of reducing the volumetric flow rate of the feed gas, which enables smaller diameter adsorption columns. It may also allow moderate vacuum pressures to be used in PVSA processes, which is preferable to pure VSA with very low desorption pressures. We note, though, that a techno-economic analysis would still be necessary to compare the pros and cons of PSA and VSA for post-combustion CO_2 capture.

We selected an additional five adsorbents for comparison to F4_MIL-140A(Ce). UTSA-16, a MOF based on Co^{II}, K^{I} and citrate, was selected due to its promising performance for post-combustion capture applications using PVSA.[44,58,59] The isotherm data used here are related to extrudates of UTSA-16.[60] CALF-20, a MOF based on Zn^{II}, oxalate and 1,2,4-triazolate, was selected due to its recent deployment in a TSA process for CO_2 capture from cement plant flue gas[41,61] and promising VSA performance.[12,62] HKUST-1,[42] a MOF based on Cu^{II} and trimesate, was selected as a representative MOF with a high surface area and porosity. Zeolite 13X and activated carbon were selected as benchmark commercial adsorbents. These decisions were also driven by the availability of isotherm data at elevated pressure for CO_2 and N_2 at least three temperatures each.[60,62–64] Our process model does not currently have the ability to consider desorption hysteresis and hysteresis loop scanning, which explains why we did not include MIL-53(Al) in this comparison. However, given the recent work by Takakura *et al.*,[20] this could present an opportunity for future work. Another factor is that the step in the CO_2 isotherm of MIL-53(Al) does not occur until very high CO_2 partial pressures at the temperatures considered in this work (6–8 bar_a at 298 K),[7] which would not be achieved even under the PSA conditions investigated here. The isotherm model parameters and example isotherms for all adsorbents considered in this work are provided in the ESI.†

The process model used in this work is a previously published adiabatic batch adsorber model,[44] based on the original work of Maring and Webley.[65] Recently, Subramanian Balashankar *et al.* highlighted the effectiveness of a light-product pressurisation (LPP) stage,[66] which we have included

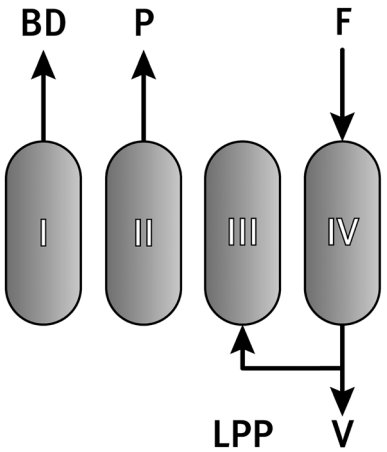

Fig. 4 The PVSA cycle simulated in this work, where: BD (blowdown), P (product), LPP (light-product pressurisation), F (feed), V (vent).

in this work. The adsorption cycle used in this work is a 4-stage cycle with blowdown and LPP (Fig. 4). The blowdown stage is used to improve CO_2 product purity at the expense of recovery, by venting weakly adsorbed gases and gas in the void space. The LPP stage increases recovery by reducing the amount of fresh feed required, by re-pressuring the bed with the waste gas vented (raffinate) during the feed stage. The published model was originally intended for operation up to 1.5 bar_a, and as such, the required gas physical properties are updated here for operation up to 10 bar_a. The model is further described in the ESI† (Section S2), and the new C_p/C_v ratio (adiabatic index) function is also provided in the ESI† (Section S2.10). We note that the model considers thermal effects arising from the enthalpy of adsorption and heat capacity of the adsorbent. Hence, changes in working capacity are captured. However, as the bed is treated as uniform, effects such as desorption being triggered at the feed end of the bed due to a temperature rise (and the corresponding impacts on bed utilisation) are not accounted for.

Another point of consideration is that this kind of batch adsorber model assumes that the breakthrough profile of the bed is a shock transition (*i.e.*, without dispersion). This is the case for convex isotherms, which the vast majority of adsorbents display. However, when an isotherm has more than one point of inflection, as is the case for stepped/gated isotherms, this can result in multipart transitions.[10,67–69] For isotherms like CO_2 on F4_MIL-140A(Ce), a shock–wave–shock transition can be displayed depending on the feed conditions. That is, a single shock transition becomes split into two smaller segments separated by a dispersed section (see Fig. S18†).[70] This increased dispersion results in more CO_2 present in the N_2 product, which diminishes the CO_2 recovery. We highlight that the assumption of a shock transition in the feed step is not fully correct in the case of stepped isotherms. This can have a strong impact on the calculated recovery of materials with a stepped isotherm, which in turn could change the ranking of adsorbents. Further investigation with a detailed dynamic model will be required in the future to substantiate these results.

We used multi-objective optimisation to compare the performance of the adsorbents. There are several parameters that can be manipulated which influence the purity and recovery obtained for each sorbent, namely, the adsorption temperature, adsorption pressure, blowdown pressure, and desorption pressure. Opting for an optimisation-based approach allows the adsorbents to be compared based on best-achievable performance (with this cycle and modelling

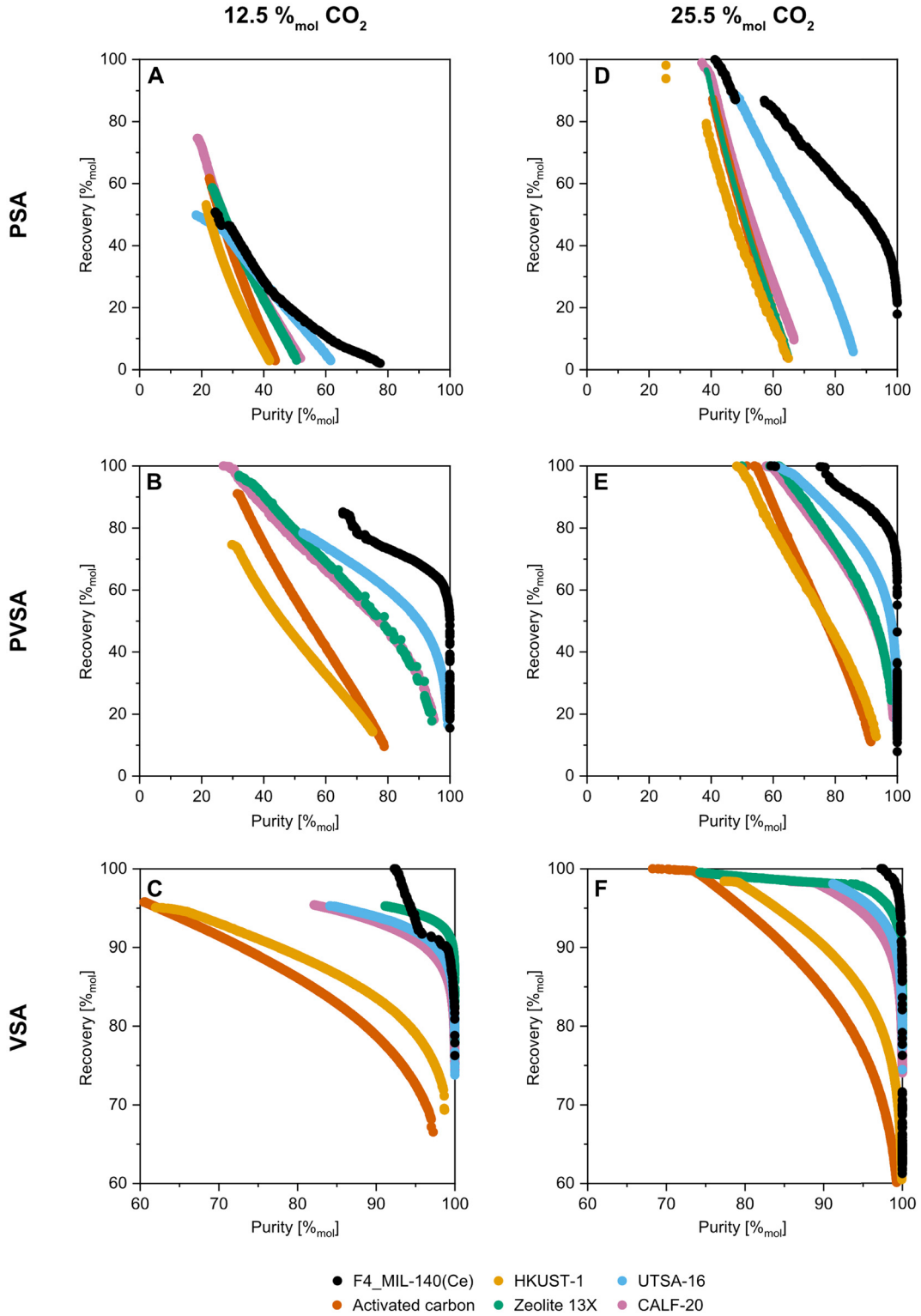

Fig. 5 Purity-recovery Pareto fronts for each adsorbent (colours), cycle types (rows), and flue gas compositions (columns) in PSA (A and D), PVSA (B and E) and VSA (C and F) conditions. Please note the different axis limits of (C) and (F). The symbol size for Zeolite 13X in (D) has been reduced to reveal the activated carbon points.

approach), as compared to a fixed set of operating conditions. For this, we use a variant of the NSGA-II algorithm implemented in MATLAB R2018b under the *gamultiobj* function with a population size of 400 and maximum generations of 50. The initial population was generated using Latin Hypercube Sampling based on the upper and lower bounds of each parameter described in Table 2. A constraint was also applied such that $P_{ads} > P_{bd} > P_{des}$. The two objective functions were the reciprocals of purity and recovery. The results from every function evaluation were logged for each scenario and adsorbent, and the Pareto curve generated by using *ParetoQS*.[71]

Adsorbent performance. The resulting Pareto curves for the six scenarios investigated are shown in Fig. 5. In the 12.5%$_{mol}$ CO_2 under PSA case (Fig. 5A), all the adsorbents considered perform fairly similarly, and aside from UTSA-16, display convex Pareto fronts. Ideally, recovery is traded-off for an improvement in purity (linear or concave Pareto fronts) by increasing the amount of blowdown carried out. In this case, additional blowdown is hampering the product purity, and this is normally due to a combination of low selectivity (due to high N_2 adsorption) and isotherm shape. As the pressure is reduced, both CO_2 and N_2 are removed in similar proportion, and the gas phase does not become enriched in CO_2. Consequently, CO_2 recovery is sacrificed for little improvement in CO_2 purity. Of the adsorbents considered, none show suitable performance under PSA conditions. Even at the higher feed gas concentration of 25.5%$_{mol}$ CO_2, some adsorbents achieve at least 90% recovery, but do not reach 95%$_{mol}$ CO_2 purity (Fig. 5D).

The impact of the step in the F4_MIL-140A(Ce) isotherm can be seen in the 12.5 and 25.5%$_{mol}$ CO_2 PSA cases, by the discontinuity in the Pareto fronts. To corroborate this, Fig. 6 displays the operating conditions selected by the optimiser. A gradual increase in the amount of blowdown is seen in Fig. 6C, reflected in the reduction of blowdown pressure in-line with reducing recovery. However, there is a step change in adsorption temperature in the higher recovery region

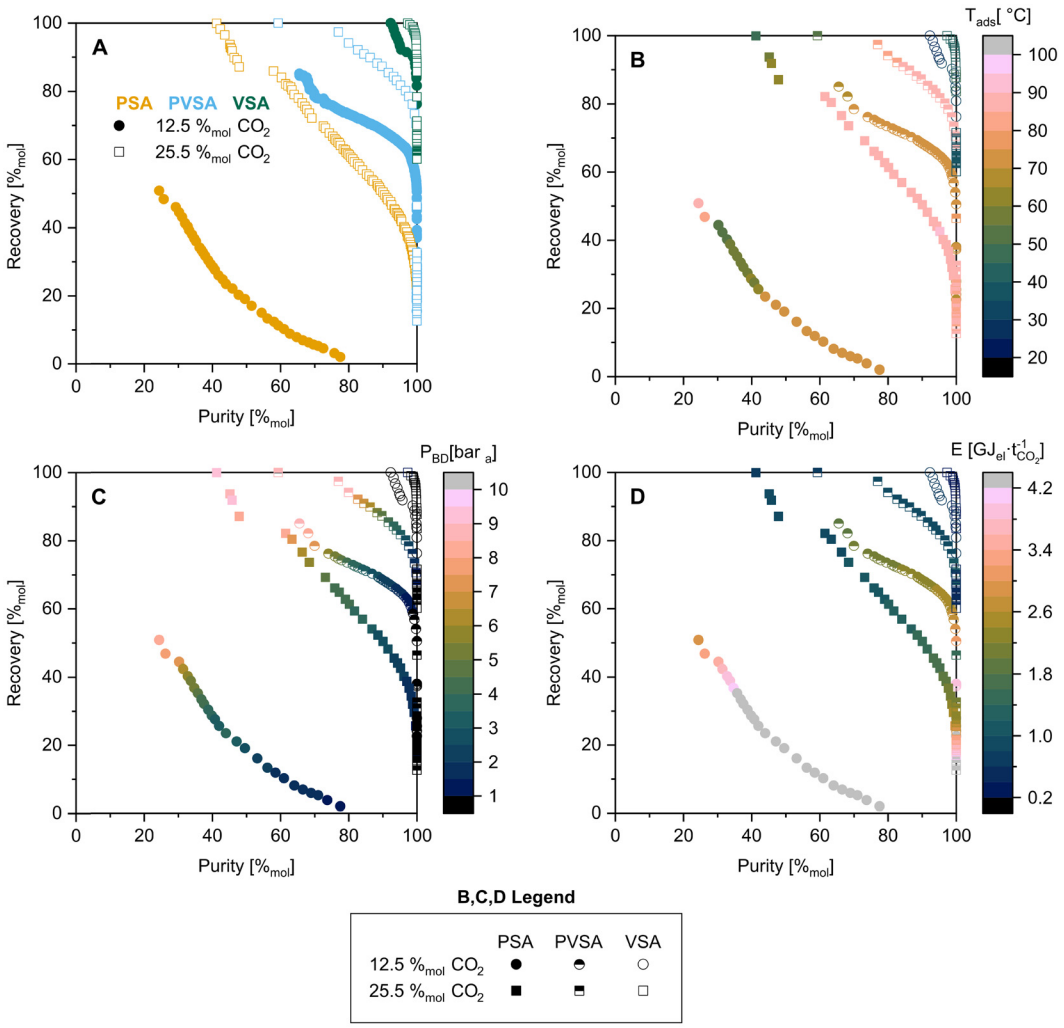

Fig. 6 Compiled Pareto fronts (A) and corresponding operating conditions for F4_MIL-140A(Ce) for each scenario; adsorption temperature (B) and blowdown pressure (C). The adsorption and desorption pressures are not shown as they are almost always at their respective limits. Specific energy consumption for F4_MIL-140A(Ce) (D). In (B), (C), and (D), some points have been skipped for improved clarity.

(Fig. 6B). This is to force the isotherm step to lower pressures such that the end of the desorption stage is at the top of the step. In such a scenario, the CO_2 working capacity and thus purity are low. However, this results in a lower feed requirement, and thus higher recovery. If this were not possible, the Pareto fronts would end at the ≈30 and ≈57%$_{mol}$ CO_2 purity marks, respectively. One could argue against the utility of such a feature, however, there are some cases where maximum recovery is key, such as in the first stage of a hybrid or multi-stage separation process.

Moving on to PVSA, the inclusion of even mild vacuum (0.3 bar$_a$) results in substantial improvement in attainable purity and recovery for all adsorbents considered (Fig. 5B and E). The performance of activated carbon and HKUST-1 is still noticeably lower than the other adsorbents, and this is due to their poor working selectivity. The zeolite 13X and HKUST-1 samples considered in this work have similar N_2 adsorption capacities at 298.15 K, so the optimiser selects higher adsorption temperatures to mitigate N_2 adsorption. At these temperatures, the HKUST-1 CO_2 isotherms become quite linear, whereas 13X retains its Langmuir-type shape. This culminates in greater CO_2 working capacity for 13X and thus greater product purity. For F4_MIL-140A(Ce), Pareto fronts for both the 12.5%$_{mol}$ CO_2 case and 25.5%$_{mol}$ CO_2 case display a discontinuity at the higher purity region. This behaviour is attributable to the same behaviour seen in the 25.5%$_{mol}$ CO_2 PSA case previously discussed.

In the VSA cases, all the adsorbents aside from activated carbon and HKUST-1 achieve the US DOE 95%$_{mol}$ CO_2 purity – 90%$_{mol}$ recovery target (Fig. 5C and F). The linear-like region in the F4_MIL-140A(Ce) Pareto fronts arises from the amount of feed required in stage IV of the cycle. The adiabatic effects during the re-pressurisation stage (stage III) result in some amount of CO_2 and N_2 in the bed at the end of the stage, which then impacts the amount of feed required in stage IV. The desorption during stages I and II cools the bed and shifts the isotherm step to low CO_2 partial pressure. At low temperatures and low CO_2 partial pressures (such as those experienced when re-pressuring with the N_2-rich light product), small changes in temperature can result in the CO_2 loading transitioning between "before the step" and "on the step". Consequently, changes in temperature at the end of stage II arising from differing adsorption temperatures and desorption amounts lead to variations in amount adsorbed at the end of stage III (when also combined with the adiabatic heat effects from adsorption). For the 12.5%$_{mol}$ CO_2 VSA case (Fig. 5C) at high CO_2 product purity (95 to >99%$_{mol}$ CO_2), zeolite 13X shows better performance than F4_MIL-140A(Ce). This is due to 13X having comparatively better CO_2 working capacity, arising from less adiabatic cooling during stages I and II, and the shape of its isotherms. In nearly all cases, the optimiser has selected the lowest possible desorption pressure (0.01 bar$_a$). The industrial implementation of such pressures with mechanical vacuum is difficult and energy intensive, especially because the efficiency of vacuum pumps reduces drastically below 0.3 bar$_a$.[72,73]

In addition to purity and recovery performance, the Pareto curves shown in Fig. 5 have been grouped by adsorbent and colour mapped by energy consumption (Fig. S21†). This is not necessarily a fair comparison, as the purity-recovery performance for all adsorbents is not on the same basis. However, it provides a qualitative overview. Overall, the energy consumption values displayed by the adsorbents are on the same order, with no clear differences. Looking at F4_MIL-140A(Ce) (Fig. 6D and S21†), improved purity-recovery performance seems to be attained at similar energy consumption values to the other adsorbents, with perhaps the exception of the 12.5%$_{mol}$ CO_2 case under VSA conditions when compared to 13X. Given the allowed bounds of the VSA process (Table 2), the step in the F4_MIL-140A(Ce) isotherm is not able to be traversed, which limits the attainable CO_2 working capacity, which in turn increases the specific energy consumption.

These findings are of course based on the simplified model used in this study, and the ranking of adsorbents may be affected by the multi-part transition that could occur in the feed step for F4_MIL-140A(Ce) and the accompanying complex thermal fronts. These results are an initial indication of the performance of F4_MIL-140A(Ce), however, further work is required to investigate the impact of the aforementioned factors on process performance.

Impact of heat capacity. To investigate the impacts of optimising process performance based on the estimated C_p, we performed a comparative study on F4_MIL-140A(Ce) for the 25.5%$_{mol}$ CO_2 case under VSA conditions. First, we conducted the optimisation using an estimated C_p value. This case is represented by the black circles in Fig. 7. The estimation method used is that described in our previous work[44] and yields a result of 748 J kg^{-1} K^{-1} at 313.15 K. At that temperature, the measured value is 824 J kg^{-1} K^{-1}. Next, taking those optimised operating conditions, the simulations were repeated with the measured/actual C_p. This case is the orange circles in Fig. 7. We performed this exercise to represent the situation where optimisation is carried out using estimated values, but then the process is operated using the 'real adsorbent'. Finally, the blue circles represent the performance if the optimisation is carried out with the measured/actual C_p in the first place. These are the same data as presented in Fig. 5F for F4_MIL-140A(Ce).

At a given purity, we observe up to a one percentage-point difference in attainable recovery. This is due to the optimiser selecting operating conditions that make the most of the isotherm step accounting for the bed thermal effects. Thus, when the adsorbent C_p is different to the value used for optimisation, the adiabatic temperature swings that occur are no longer the most ideal. However, if actual C_p data are available, and optimisation is carried out with those data, a compromise can be achieved with adjustment in the operating conditions. In the case of F4_MIL-140A(Ce), the impacts are small due to two factors. First, there is a reasonable match between the estimated C_p and the measured C_p (possibly fortuitous), which allows the optimiser

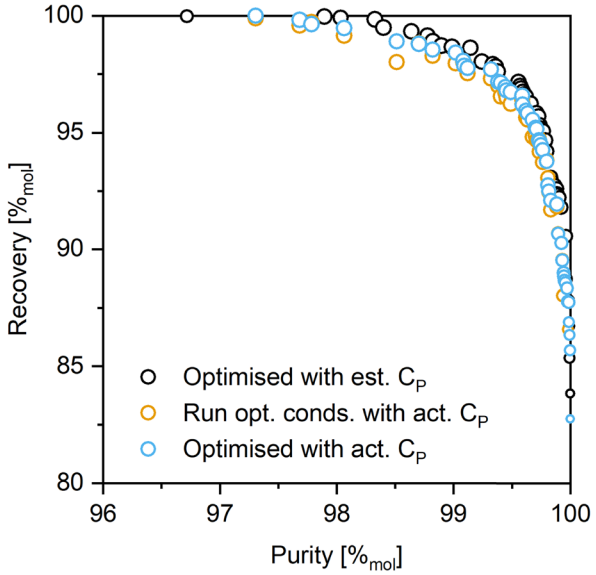

Fig. 7 Impact of performing optimisation with estimated C_p on F4_MIL-140A(Ce) for the 25.5%$_{mol}$ CO_2 case under VSA conditions. Black symbols are optimisation undertaken with estimated heat capacity. Orange symbols are process performance based on the operating conditions determined with estimated heat capacity (previous case) but the measured/actual C_p is used. Blue symbols represent results if optimisation is carried out with the measured heat capacity directly (the same data from black symbols in Fig. 5F). The size of the symbols is proportional to the CO_2 working capacity.

to find ideal operating conditions within the allowed bounds. In the case that there was a significant difference, it is possible that the ideal operating conditions would be outside the pre-defined allowed range. Secondly, F4_MIL-140A(Ce) has a low Q_{ads} for CO_2 and a small shift in isotherm step with temperature; these are ideal characteristics to minimise the impacts of this issue. It should be noted that the scenario with the greatest impact (*i.e.*, the worst case scenario) is shown here. That is, the one that experiences the greatest adiabatic temperature swings during desorption and re-pressurisation. In the 12.5%$_{mol}$ CO_2 case under PSA conditions (Fig. 5D), there is an insignificant deviation between the three Pareto curves for F4_MIL-140A(Ce).

A recent study considered the impacts of C_p variation on the energy consumption of TSA processes.[47] The outcomes are mostly as expected, with increased C_p resulting in increased energy requirements, but the relationship appears non-linear or unpredictable. This is likely due to the relative contributions of sensible heating and enthalpy of ad/desorption to the regeneration energy. For a fixed temperature swing, adsorbents with a high C_p and Q_{ads} can have a much greater proportion of their regeneration energy requirements attributed to adsorbate desorption. On the other hand, an adsorbent with high C_p, low Q_{ads}, and small working capacity will be impacted by variation in C_p to a greater extent. The same phenomenon also exists for adiabatic processes, such that, some adsorbent–adsorbate combinations will have different sensitivities to variation in C_p due to the aforementioned factors. In that vein, F4_MIL-140A(Ce) does not appear extremely sensitive to this, as the shift in the step pressure with temperature is relatively small. This is in contrast to amine-functionalised adsorbents where the shift in step pressure with temperature can be large,[6] and the corresponding impacts of adiabatic process operation can be significant.[26] The issue is further exacerbated by their high CO_2 Q_{ads}, which gives rise to significant temperature swings that can cause a sudden release of adsorbed CO_2. This phenomenon results in a significant portion of the adsorbent bed being underutilised, as it has to be reserved to prevent the released CO_2 from being lost to the raffinate/outlet.[25]

Conclusions

The PVSA process optimisation presented in this work suggests that the "phase-change" MOF F4_MIL-140A(Ce), which displays a non-hysteretic step-shaped CO_2 adsorption isotherm, has the potential to be an effective adsorbent for post-combustion CO_2 capture from relatively high concentration streams (12.5 vol% and 25.5 vol%). In nearly all cases considered with the methodology employed, the predicted performance of F4_MIL-140A(Ce) is better, in terms of recovery and purity, compared to the other adsorbents (zeolite 13X, activated carbon, UTSA-16, CALF-20, and HKUST-1). Such a good performance is enabled by the step-shaped isotherm that leads to saturation over a narrow range of CO_2 partial pressures compatible with those found in the targeted streams.

We should reiterate that the model used in this work is a simplified one and does not capture the column dynamics. Information on column dynamics is necessary to understand the impacts of the multi-part transition that may occur for F4_MIL-140A(Ce) during the adsorption step and hamper recovery. The accompanied complex thermal effects are also not captured, as well as the corresponding impacts on bed utilisation. Overall, the present model is useful to capture trends and screen potential adsorbents, however, the adsorbent ranking presented here would need to be validated with a detailed model in future work.

We also presented a methodology to obtain a reliable measurement of the C_p of F4_MIL-140A(Ce) by DSC in the 285–480 K temperature range, which involves the use of a pellet of the poorly thermally conductive MOF dispersed in a matrix of activated alumina. The impact of using a calculated value of C_p *versus* the experimentally determined one on the results of process optimisation was evaluated, finding that in the case of F4_MIL-140A(Ce) there is a limited difference in the achievable recovery/purity. This mild effect mainly results from the relatively low Q_{ads} displayed by this MOF, combined with the small shifts of the isotherm step in response to temperature changes.

The next steps required to fully evaluate the relative merits and demerits of an adsorbent such as F4_MIL-140A(Ce) for post-combustion CO_2 capture include multi-component dynamic column breakthrough measurements and rigorous process modelling with techno-economic analysis. Of special

interest is the evaluation of the separation performance in the presence of humidity, given the strong affinity of the adsorption sites in F4_MIL-140A(Ce) for water, which might displace CO_2.

Experimental section

Materials

Cerium(IV) ammonium nitrate (16774-21-3, 99%, $Ce(NH_4)_2(NO_3)_6$, Sigma-Merck), nitric acid (7697-37-2, 68%, HNO_3, Sigma-Merck), tetrafluoroterephthalic acid (652-36-8, 97%, $C_8H_2F_4O_4$, Fluorochem). All reagents were used as received, with no further purification.

Synthesis of F4_MIL-140A(Ce)

F4_MIL-140A(Ce) was synthesised following a literature procedure:[34] tetrafluoroterephthalic acid (179 mg, 0.75 mmol) was dissolved in water (10.5 mL) and 16 mol L^{-1} HNO_3 (1.5 mL, 24 mmol) in a 20 mL scintillation vial, which was kept at 60 °C under stirring in an aluminium heating block. After 10 minutes, a solution of cerium(IV) ammonium nitrate (411 mg, 0.75 mmol) in water (3 mL) was added into the vial and the mixture was left to react for 1 h. At the end of the reaction, the yellow solid was centrifuged, washed twice with water (15 mL each time) and finally washed with acetone (15 mL). The solid was dried in an oven at 80 °C. Yield: 177 mg (60%).

Gas adsorption volumetry

CO_2 and N_2 adsorption–desorption isotherms up to 5 bar were measured with a Quantachrome iSorb High Pressure Gas Analyser at 298 K (both gases), 313 K (both gases), 328 K (both gases) and 343 K (CO_2). About 200 mg of sample was used for the adsorption studies. The sample was degassed at 393 K under dynamic vacuum for 12 h prior to analysis and at 393 K for 1 h in between subsequent measurements.

Thermogravimetric analysis (TGA)

TGA of F4_MIL-140A(Ce) was performed with a TA Instruments Thermobalance model Q5000IR using a heating rate of 10 K min^{-1} in the temperature range of 303–523 K under nitrogen flow (25 mL min^{-1}). The amount of sample was 2.157 mg. Mass calibration was performed using certified mass standards, in the range 0–100 mg, supplied by TA Instruments. Temperature calibration was based on the Curie point of paramagnetic metals. A multi-point calibration with five Curie point reference materials (Alumel, Ni, Ni83%Co17%, Ni63%Co37%, and Ni37%Co63%) was performed.

Differential scanning calorimetry (DSC)

DSC analyses were carried out using a TA Instruments Discovery DSC model 250 under nitrogen gas flow (50 mL min^{-1}) on F4_MIL-140A(Ce) in different forms: (i) powder; (ii) thin pellet; (iii) dispersed within a matrix of activated alumina (10 and 20 wt% of F4_MIL-140A(Ce)). The masses of each sample used in DSC experiments are reported in the following table (Table 3):

Aluminium DSC pans with a pin hole lid were used to allow the water evaporation during the first heating ramp.

The method adopted is the classic three run heat capacity method discussed in ASTM E1269. Baseline, reference (sapphire) and samples were analysed by using the following method:

– Equilibrate to 273.15 K.
– Isothermal 3 min.
– Ramp 10 K min^{-1} to 483.15 K.
– Isothermal 10 min.
– Ramp 20 K min^{-1} to 273.15 K.
– Isothermal 10 min.
– Ramp 10 K min^{-1} to 483.15 K.
– Isothermal 10 min.
– Ramp 20 K min^{-1} to 273.15 K.
– Isothermal 10 min.
– Ramp 10 K min^{-1} to 483.15 K.

The first heating scan up to 483.15 K was conducted to evaporate the superficial and structural water of F4_MIL-140A(Ce) and activated alumina.

To obtain the most accurate C_p value, pan/lid combinations for all runs was cleaned and their weight matched to a precision of +0.01 mg.

The DSC was calibrated with indium, and an empty pan was used as a reference.

The determination of C_p of F4_MIL-140A(Ce) powders and pellets, activated alumina pellet, and F4_MIL-140A(Ce) dispersed in activated alumina pellet was performed by comparing the difference between the sample's heat flow

Table 3 Mass, form and name of the samples subjected to DSC analysis

Sample	Form	Mass[a] (mg)
F4_MIL-140A(Ce)	Powder	1.85
F4_MIL-140A(Ce)	Powder	4.15
F4_MIL-140A(Ce)	Thin pellet	1.84
F4_MIL-140A(Ce)	Thin pellet	4.06
Activated alumina	Pellet	19.33
Activated alumina/F4_MIL-140A(Ce)	Pellet	36.65 (AA = 33.16; MOF = 3.49)
Activated alumina/F4_MIL-140A(Ce)	Pellet	36.43 (AA = 29.53; MOF = 6.90)

[a] The reported masses refer to the dry mass of the sample calculated by subtracting the water content determined by TGA analysis.

signal and the sapphire reference's heat flow signal relative to a common heat flow baseline, according to eqn (1):

$$C_p(T) = \frac{\text{Heat flow}_{sample} - \text{Heat flow}_{baseline}}{\text{Heat flow}_{sapphire} - \text{Heat flow}_{baseline}} \times C_{p_{sapphire}} \quad (1)$$

The $C_{P_{sapphire}}$, as a function of the temperature, was calculated by the Shomate equation according to parameters given in ref. 74.

The C_p of F4_MIL-140A(Ce) dispersed in the activated alumina matrix was determined by simply considering the C_p as an additive, according to eqn (2):

$$C_p(T)\text{MOF} = \frac{\left(C_{p_{AA/MOF}} \cdot m_{AA/MOF} - C_{p_{AA}} \cdot m_{AA}\right)}{m_{MOF}} \quad (2)$$

where $C_{p_{AA/MOF}}$ and $m_{AA/MOF}$ are the C_p of the AA/MOF sample calculated according to eqn (2) and its mass, respectively, m_{AA} and m_{MOF} are the mass of activated alumina and MOF in the AA/MOF sample.

Conflicts of interest

There are no conflicts of interest to declare.

Acknowledgements

M. T. thanks the University of Pisa for the provision of funding through the Progetto di Ricerca di Ateneo scheme (PRA_2020_39). D. D. and C. P. would like to acknowledge funding from Research Councils UK (RCUK) under grants EP/P026214/1 and EP/T033940/1. The Scientific colour map batlow[75] is used in this study to prevent visual distortion of the data and exclusion of readers with colourvision deficiencies.[76]

References

1 M. Bui, C. S. Adjiman, A. Bardow, E. J. Anthony, A. Boston, S. Brown, P. S. Fennell, S. Fuss, A. Galindo, L. A. Hackett, J. P. Hallett, H. J. Herzog, G. Jackson, J. Kemper, S. Krevor, G. C. Maitland, M. Matuszewski, I. S. Metcalfe, C. Petit, G. Puxty, J. Reimer, D. M. Reiner, E. S. Rubin, S. A. Scott, N. Shah, B. Smit, J. P. M. Trusler, P. Webley, J. Wilcox and N. Mac Dowell, *Energy Environ. Sci.*, 2018, **11**, 1062–1176.

2 H. A. Patel, J. Byun and C. T. Yavuz, *ChemSusChem*, 2017, **10**, 1303–1317.

3 M. Oschatz and M. Antonietti, *Energy Environ. Sci.*, 2018, **11**, 57–70.

4 K. Sumida, D. L. Rogow, J. A. Mason, T. M. McDonald, E. D. Bloch, Z. R. Herm, T.-H. Bae and J. R. Long, *Chem. Rev.*, 2012, **112**, 724–781.

5 Z. Hu, Y. Wang, B. B. Shah and D. Zhao, *Adv. Sustainable Syst.*, 2019, **3**, 1800080.

6 T. M. McDonald, J. A. Mason, X. Kong, E. D. Bloch, D. Gygi, A. Dani, V. Crocellà, F. Giordanino, S. O. Odoh, W. S. Drisdell, B. Vlaisavljevich, A. L. Dzubak, R. Poloni, S. K. Schnell, N. Planas, K. Lee, T. Pascal, L. F. Wan, D. Prendergast, J. B. Neaton, B. Smit, J. B. Kortright, L. Gagliardi, S. Bordiga, J. A. Reimer and J. R. Long, *Nature*, 2015, **519**, 303–308.

7 A. Boutin, F.-X. Coudert, M.-A. Springuel-Huet, A. V. Neimark, G. Férey and A. H. Fuchs, *J. Phys. Chem. C*, 2010, **114**, 22237–22244.

8 D. Li and K. Kaneko, *Chem. Phys. Lett.*, 2001, **335**, 50–56.

9 C. O. Ania, E. García-Pérez, M. Haro, J. J. Gutiérrez-Sevillano, T. Valdés-Solís, J. B. Parra and S. Calero, *J. Phys. Chem. Lett.*, 2012, **3**, 1159–1164.

10 M. Hefti, L. Joss, Z. Bjelobrk and M. Mazzotti, *Faraday Discuss.*, 2016, **192**, 153–179.

11 X. Yao, K. E. Cordova and Y.-B. Zhang, *Small Struct.*, 2022, **3**, 2100209.

12 T. T. T. Nguyen, G. K. H. Shimizu and A. Rajendran, *Chem. Eng. J.*, 2023, **452**, 139550.

13 T. D. Burns, K. N. Pai, S. G. Subraveti, S. P. Collins, M. Krykunov, A. Rajendran and T. K. Woo, *Environ. Sci. Technol.*, 2020, **54**, 4536–4544.

14 A. K. Rajagopalan, A. M. Avila and A. Rajendran, *Int. J. Greenhouse Gas Control*, 2016, **46**, 76–85.

15 D. Yancy-Caballero, K. T. Leperi, B. J. Bucior, R. K. Richardson, T. Islamoglu, O. K. Farha, F. You and R. Q. Snurr, *Mol. Syst. Des. Eng.*, 2020, **5**, 1205–1218.

16 X. Zhang, T. Zhou and K. Sundmacher, *AIChE J.*, 2022, **68**, e17524.

17 M. Khurana and S. Farooq, *Chem. Eng. Sci.*, 2016, **152**, 507–515.

18 R. Ben-Mansour, O. E. Bamidele and M. A. Habib, *Int. J. Energy Res.*, 2015, **39**, 1994–2007.

19 I. Majchrzak-Kucęba, D. Wawrzyńczak and A. Ściubidło, *Fuel*, 2019, **255**, 115773.

20 Y. Takakura, S. Sugimoto, J. Fujiki, H. Kajiro, T. Yajima and Y. Kawajiri, *ACS Sustainable Chem. Eng.*, 2022, **10**, 14935–14947.

21 T. M. McDonald, W. R. Lee, J. A. Mason, B. M. Wiers, C. S. Hong and J. R. Long, *J. Am. Chem. Soc.*, 2012, **134**, 7056–7065.

22 R. L. Siegelman, T. M. McDonald, M. I. Gonzalez, J. D. Martell, P. J. Milner, J. A. Mason, A. H. Berger, A. S. Bhown and J. R. Long, *J. Am. Chem. Soc.*, 2017, **139**, 10526–10538.

23 A. C. Forse, P. J. Milner, J.-H. Lee, H. N. Redfearn, J. Oktawiec, R. L. Siegelman, J. D. Martell, B. Dinakar, L. B. Porter-Zasada, M. I. Gonzalez, J. B. Neaton, J. R. Long and J. A. Reimer, *J. Am. Chem. Soc.*, 2018, **140**, 18016–18031.

24 E. J. Kim, R. L. Siegelman, H. Z. H. Jiang, A. C. Forse, J.-H. Lee, J. D. Martell, P. J. Milner, J. M. Falkowski, J. B. Neaton, J. A. Reimer, S. C. Weston and J. R. Long, *Science*, 2020, **369**, 392.

25 K. N. Pai, J. D. Baboolal, D. A. Sharp and A. Rajendran, *Sep. Purif. Technol.*, 2019, **211**, 540–550.

26 R. Hughes, G. Kotamreddy, A. Ostace, D. Bhattacharyya, R. L. Siegelman, S. T. Parker, S. A. Didas, J. R. Long, B. Omell and M. Matuszewski, *Energy Fuels*, 2021, **35**, 6040–6055.

27 H. Kajiro, A. Kondo, K. Kaneko and H. Kanoh, *Int. J. Mol. Sci.*, 2010, **11**, 3803–3845.

28 F. J. Sotomayor and C. M. Lastoskie, *Microporous Mesoporous Mater.*, 2020, **304**, 110377.
29 S. Hiraide, Y. Sakanaka, H. Kajiro, S. Kawaguchi, M. T. Miyahara and H. Tanaka, *Nat. Commun.*, 2020, **11**, 3867.
30 M. Ichikawa, A. Kondo, H. Noguchi, N. Kojima, T. Ohba, H. Kajiro, Y. Hattori and H. Kanoh, *Langmuir*, 2016, **32**, 9722–9726.
31 C. Serre, F. Millange, C. Thouvenot, M. Noguès, G. Marsolier, D. Louër and G. Férey, *J. Am. Chem. Soc.*, 2002, **124**, 13519–13526.
32 T. Loiseau, C. Serre, C. Huguenard, G. Fink, F. Taulelle, M. Henry, T. Bataille and G. Férey, *Chem. – Eur. J.*, 2004, **10**, 1373–1382.
33 R. D'Amato, A. Donnadio, M. Carta, C. Sangregorio, D. Tiana, R. Vivani, M. Taddei and F. Costantino, *ACS Sustainable Chem. Eng.*, 2019, **7**, 394–402.
34 S. J. I. Shearan, J. Jacobsen, F. Costantino, R. D'Amato, D. Novikov, N. Stock, E. Andreoli and M. Taddei, *Chem. – Eur. J.*, 2021, **27**, 6579–6592.
35 M. Cavallo, C. Atzori, M. Signorile, F. Costantino, D. M. Venturi, A. Koutsianos, K. A. Lomachenko, L. Calucci, F. Martini, A. Giovanelli, M. Geppi, V. Crocellà and M. Taddei, *J. Mater. Chem. A*, 2023, **11**, 5568–5583.
36 P. Mishra, H. P. Uppara, B. Mandal and S. Gumma, *Ind. Eng. Chem. Res.*, 2014, **53**, 19747–19753.
37 L. Hamon, P. L. Llewellyn, T. Devic, A. Ghoufi, G. Clet, V. Guillerm, G. D. Pirngruber, G. Maurin, C. Serre, G. Driver, W. van Beek, E. Jolimaître, A. Vimont, M. Daturi and G. Férey, *J. Am. Chem. Soc.*, 2009, **131**, 17490–17499.
38 T. R. C. Van Assche, G. V. Baron and J. F. M. Denayer, *Dalton Trans.*, 2016, **45**, 4416–4430.
39 V. M. Georgieva, E. L. Bruce, M. C. Verbraeken, A. R. Scott, W. J. Casteel Jr., S. Brandani and P. A. Wright, *J. Am. Chem. Soc.*, 2019, **141**, 12744–12759.
40 C. A. Grande, R. Blom, V. Middelkoop, D. Matras, A. Vamvakeros, S. D. M. Jacques, A. M. Beale, M. Di Michiel, K. A. Andreassen and A. M. Bouzga, *Chem. Eng. J.*, 2020, **402**, 126166.
41 J.-B. Lin, T. T. T. Nguyen, R. Vaidhyanathan, J. Burner, J. M. Taylor, H. Durekova, F. Akhtar, R. K. Mah, O. Ghaffari-Nik, S. Marx, N. Fylstra, S. S. Iremonger, K. W. Dawson, P. Sarkar, P. Hovington, A. Rajendran, T. K. Woo and G. K. H. Shimizu, *Science*, 2021, **374**, 1464–1469.
42 S. S.-Y. Chui, S. M.-F. Lo, J. P. H. Charmant, A. G. Orpen and I. D. Williams, *Science*, 1999, **283**, 1148–1150.
43 H. Wu, W. Zhou and T. Yildirim, *J. Am. Chem. Soc.*, 2009, **131**, 4995–5000.
44 D. Danaci, M. Bui, N. M. Dowell and C. Petit, *Mol. Syst. Des. Eng.*, 2020, **5**, 212–231.
45 A. H. Farmahini, S. Krishnamurthy, D. Friedrich, S. Brandani and L. Sarkisov, *Chem. Rev.*, 2021, **121**, 10666–10741.
46 M. Taddei and C. Petit, *Mol. Syst. Des. Eng.*, 2021, **6**, 841–875.
47 S. M. Moosavi, B. Á. Novotny, D. Ongari, E. Moubarak, M. Asgari, Ö. Kadioglu, C. Charalambous, A. Ortega-Guerrero, A. H. Farmahini, L. Sarkisov, S. Garcia, F. Noé and B. Smit, *Nat. Mater.*, 2022, **21**, 1419–1425.
48 J. Wieme, S. Vandenbrande, A. Lamaire, V. Kapil, L. Vanduyfhuys and V. Van Speybroeck, *ACS Appl. Mater. Interfaces*, 2019, **11**, 38697–38707.
49 H. Sugiura, H. Kajiro and H. Kanoh, *Colloids Surf., A*, 2022, **651**, 129745.
50 J. Rumble, *CRC Handbook of Chemistry and Physics*, CRC Press, Boca Raton, FL, 100th edn, 2019.
51 B. T. Goodman, W. V. Wilding, J. L. Oscarson and R. L. Rowley, *J. Chem. Eng. Data*, 2004, **49**, 24–31.
52 N. Querejeta, S. García, N. Álvarez-Gutiérrez, F. Rubiera and C. Pevida, *J. CO2 Util.*, 2019, **33**, 148–156.
53 B. Mu and K. S. Walton, *J. Phys. Chem. C*, 2011, **115**, 22748–22754.
54 F. A. Kloutse, R. Zacharia, D. Cossement and R. Chahine, *Microporous Mesoporous Mater.*, 2015, **217**, 1–5.
55 D. Liu, J. J. Purewal, J. Yang, A. Sudik, S. Maurer, U. Mueller, J. Ni and D. J. Siegel, *Int. J. Hydrogen Energy*, 2012, **37**, 6109–6117.
56 Y. Luo, W. Cui, Y. Zou, H. Chu, F. Xu and L. Sun, *J. Therm. Anal. Calorim.*, 2020, **142**, 891–898.
57 R. W. Powell, C. Y. Ho and P. E. Liley, *Thermal Conductivity of Selected Materials*, National Bureau of Standards, 1966.
58 A. Masala, J. G. Vitillo, G. Mondino, C. A. Grande, R. Blom, M. Manzoli, M. Marshall and S. Bordiga, *ACS Appl. Mater. Interfaces*, 2017, **9**, 455–463.
59 M. Khurana and S. Farooq, *AIChE J.*, 2019, **65**, 184–195.
60 V. I. Agueda, J. A. Delgado, M. A. Uguina, P. Brea, A. I. Spjelkavik, R. Blom and C. Grande, *Chem. Eng. Sci.*, 2015, **124**, 159–169.
61 O. Ghaffari-Nik, L. Mariac, A. Liu, B. Henkel, S. Marx and P. Hovington, Rapid Cycle Temperature Swing Adsorption Process Using Solid Structured Sorbent for CO2 capture from Cement Flue Gas, *15th International Conference on Greenhouse Gas Control Technologies, GHGT-15*, 2021.
62 T. T. T. Nguyen, J.-B. Lin, G. K. H. Shimizu and A. Rajendran, *Chem. Eng. J.*, 2022, **442**, 136263.
63 Z. Liang, M. Marshall and A. L. Chaffee, *Energy Fuels*, 2009, **23**, 2785–2789.
64 S. Cavenati, C. A. Grande and A. E. Rodrigues, *J. Chem. Eng. Data*, 2004, **49**, 1095–1101.
65 B. J. Maring and P. A. Webley, *Int. J. Greenhouse Gas Control*, 2013, **15**, 16–31.
66 V. S. Balashankar, A. K. Rajagopalan, R. de Pauw, A. M. Avila and A. Rajendran, *Ind. Eng. Chem. Res.*, 2019, **58**, 3314–3328.
67 W. Zhang, Y. Shan and A. Seidel-Morgenstern, *J. Chromatogr. A*, 2006, **1107**, 216–225.
68 F. Ortner, S. Jermann, L. Joss and M. Mazzotti, *Ind. Eng. Chem. Res.*, 2015, **54**, 11420–11437.
69 L. A. Darunte, T. Sen, C. Bhawanani, K. S. Walton, D. S. Sholl, M. J. Realff and C. W. Jones, *Ind. Eng. Chem. Res.*, 2019, **58**, 366–377.
70 J. Fujiki, H. Kajiro, Y. Takakura, T. Yajima and Y. Kawajiri, *Chem. Eng. J.*, 2023, **460**, 141781.
71 R. Tom, Find multi-objective Pareto front using modified quicksort (**https://www.mathworks.com/matlabcentral/fileexchange/73089-find-multi-objective-pareto-front-using-**

modified-quicksort), MATLAB Central File Exchange, Retrieved April 9, 2021.
72 R. T. Maruyama, K. N. Pai, S. G. Subraveti and A. Rajendran, *Int. J. Greenhouse Gas Control*, 2020, **93**, 102902.
73 D. Danaci, P. A. Webley and C. Petit, *Front. Chem. Eng.*, 2021, **2**, 602430.
74 M. W. Chase Jr., *NIST-JANAF Thermochemical Tables*, 4th edn, 1998; *J. Phys. Chem. Ref. Data, Monograph*, **9**.
75 F. Crameri, *Scientific colour maps*, Zenodo, 2018, DOI: **10.5281/zenodo.1243862**.
76 F. Crameri, G. E. Shephard and P. J. Heron, *Nat. Commun.*, 2020, **11**, 5444.